Advances in continuously profiling the thermodynamic state of the boundary layer: Integration of measurements and methods

ULRICH LÖHNERT*, S. CREWELL*, O. KRASNOV**, E. O'CONNOR***, H. RUSSCHENBERG**

*Institute for Meteorology and Geophysics, University of Cologne, GER

** Delft University of Technology, NL

***University of Reading, UK

Corresponding Author Address:

Dr. Ulrich Löhnert

Institute for Meteorology and Geophysics

Zülpicher Straße 49a

50674 Köln

Germany

Tel: +49 +221 470 1779

Fax: +49 +221 470 5161

Email: loehnert@meteo.uni-koeln.de

2 **Abstract**

3 This paper describes advances in ground based thermodynamic profiling of the lower

4 troposphere through sensor synergy. The well documented Integrated Profiling Technique

5 (IPT), which uses a microwave profiler, a cloud radar and a ceilometer to simultaneously

6 retrieve vertical profiles of temperature, humidity and liquid water content of non-

7 precipitating clouds, is further developed towards an enhanced performance in the boundary

8 layer and lower troposphere. For a more accurate temperature profile, this is accomplished by

9 including an elevation scanning measurement modus of the microwave profiler. Height

10 dependent RMS accuracies of temperature (humidity) ranging from ~0.3 to 0.9 K (0.5 to 0.8

11 gm^{-3}) in the boundary layer are derived from retrieval simulations and confirmed

12 experimentally with measurements at distinct heights taken during the LAUNCH 2005

13 campaign at the experimental site Lindenberg of the German Weather Service. Temperature

14 inversions, especially of the lower boundary layer, are captured in a very satisfactory way by

15 using the elevation scanning mode. In order to improve the quality of liquid water content

16 measurements in clouds we incorporate a sophisticated target classification scheme developed

17 within the European cloud observing network Cloudnet. It allows the detailed discrimination

18 between different types of backscatterers detected by cloud radar and ceilometer. Finally, to

19 allow IPT application also to drizzling cases, we integrate an LWC profiling method. This

20 technique classifies the detected hydrometeors into three different size classes using certain

21 thresholds determined by radar reflectivity and/or ceilometer extinction profiles. By inclusion

22 into IPT, the retrieved profiles are made consistent with the measurements of the microwave

23 profiler and a LWC a priori profile. Results of IPT application to 13 days of the LAUNCH

24 campaign are analysed and the importance of integrated profiling for model evaluation is

25 underlined.

26

1. Introduction

Continuous profiling of the thermodynamic state of the atmosphere is becoming more and more important in support of meso-scale models which are increasingly employed for Numerical Weather Prediction (NWP). Especially the development of the boundary layer (BL), e.g. its diurnal cycle or its influence on the initiation of convection, is crucial for the correct prediction of regional weather scales, including severe events such as extreme precipitation. In this context the operational radiosonde network with its typically 12-hourly observations is by far not sufficient for evaluating model performance on small time (short-term 0-+18 h) and spatial (model resolution < 3 km) scale. Because also satellites instruments are not able to resolve BL variables well, strong efforts have been undertaken within the last decade to enhance the development of ground-based remote sensing instrumentation. However, no single instrument is capable to observe all relevant atmospheric variables needed to investigate BL processes in detail. These are extremely relevant for assessing the performance of NWP models, as well as for investigating the potential for data assimilation of such observations. Therefore we describe an instrument combination method which is capable of continuously profiling the lower troposphere with special emphasis on an accurate boundary layer description.

The technique described here is an advancement of the Integrated Profiling Technique (IPT) described and assessed by Löhnert et al. 2004 (L04), respectively Löhnert et al. 2007 (L07). It combines measurements of a microwave profiler, a cloud radar and a ceilometer with suited a priori information to determine profiles of temperature (T), water vapor density (ρ_v) and cloud liquid water content (LWC) in a *physically consistent way*. This means that the retrieved profiles in state space can be transformed back into measurement space to match the original measurements within the assumed range of error. The major improvements compared to L04 which will be presented in this paper are the following:

52   1.) Instead of using only zenith observations from the Microwave Profiler (MWP), we

53   now additionally include elevation scanning measurements which can increase the

54   accuracy of the temperature profile significantly in the BL (Crewell and Löhnert

55   2007).

56   2.) We now employ the well established Cloudnet target classification scheme (Hogan

57   and O'Connor 2006) developed at the University of Reading. This scheme allows for

58   the discrimination between different hydrometeor categories, aerosols and insects

59   when profiling the atmosphere with a ceilometer and a cloud radar. It is of essential

60   value when applying a physically consistent method.

61   3.) In order to enable the applicability of the IPT to drizzling cases, we incorporate the

62   LWC profiling method according to Krasnov and Russchenberg (2006, K06) into the

63   IPT. This is a stand-alone method to determine the LWC profile in non-drizzling to

64   heavy-drizzling clouds using cloud radar and ceilometer measurements. By

65   incorporating it into the IPT, we expand the IPT applicability from non-precipitating

66   to drizzling clouds. Through incorporation into IPT, the results of K06 are made

67   physically consistent with the rest of the measurements.

68   The paper is organized as follows: In section 2 we describe the experimental setup of

69   instruments used for this study during the LAUNCH campaign. Section 3 describes the

70   improved IPT, with special emphasis on the target classification, the inclusion of the elevation

71   scanning measurements of the MWP and the incorporation of the K06 retrieval algorithm. We

72   then show results of IPT application to simulated measurements in Section 4, making clear

73   the potential of elevation scanning measurements for BL-profiling. Section 5 shows

74   experimental results obtained from comparisons with in situ radiosonde and mast

75   measurements. We also emphasize the importance of continuous measurements of

76 thermodynamic profiles by showing first comparisons with the operational NWP model

77 "Lokal-Modell" (LME) of the German Weather Service (DWD).

78 **2. Experimental Measurement Setup**

79 The measurements used in this study were all part of the LAUNCH (International **L**indenberg

80 campaign for **A**ssessment of H**U**midity a**N**d **C**loud Profiling Systems and its Impact on **H**igh-

81 Resolution Modelling) 2005 campaign at and around the Richard-Aßmann Observatory of

82 DWD at Lindenberg, Germany (52.17° N, 14.12° E). This campaign was chosen because

83 here, a MWP with an elevation scanning capability of high accuracy was operated

84 simultaneously with a cloud radar and a ceilometer. These measurements were carried out at

85 the DWD boundary layer measurement site Falkenberg about 4 km south of Lindenberg. The

86 area around Lindenberg and Falkenberg is dominated by farmland and varies between 50 and

87 120 m altitude above sea level. Additionally at the Lindenberg site, four times a day (0000,

88 0600, 1200 and 1800 UTC) operationally launched Vaisala RS-92 radiosondes are used as a

89 priori information and for accuracy assessment.

90 **2.1. Microwave Profiler**

91 The central instrument of the applied Integrated Profiling Technique (IPT) is the 14 channel

92 **H**umidity **A**nd **T**emperature microwave **PRO**filer (HATPRO, Rose et al. (2005),

93 *www.radiometer-physics.de*) that was designed as a network-suitable low-cost microwave

94 radiometer which can observe liquid water path (LWP), humidity and temperature profiles

95 with high (1s) temporal resolution. HATPRO comprises total-power radiometers utilizing

96 direct detection receivers within two bands. Band A contains seven channels from 22.335 to

97 31.4 GHz and Band B contains seven channels from 51 to 58 GHz. The channels of Band A

98 are not only suited for determining LWP, but also contain limited information about the

99 vertical profile of humidity through the pressure broadening of the optically thin 22.235 GHz

100 H_2O line. The channels of Band B, on the other hand, contain information on the vertical

101 profile of temperature. At the opaque centre of the O_2 absorption complex most of the

102 information originates from near the surface, whereas further away from the line, the

103 atmosphere becomes less and less opaque so that more and more information also originates

104 from higher atmospheric layers.

105 In addition to the spectral information, angular information can enhance the accuracy of the

106 temperature profile in the boundary layer. Therefore one channel systems operating around 60

107 GHz have been developed (Kadygrov and Pick (1998)) that derive profile information from

108 elevation scanning. Due to the fact that the atmosphere is optically thick around 60 GHz, the

109 observed radiation systematically originates from higher altitudes the higher the elevation

110 angle. This information gain can be used for profile retrieval if one assumes horizontal

111 homogeneity. Since these brightness temperatures vary only slightly with elevation angle, the

112 method requires a highly sensitive radiometer which is typically realized by using wide

113 bandwidths up to 4 GHz. For the HATPRO radiometer, Crewell and Löhnert (2007) have

114 shown on the basis of statistical algorithms that, considering Band B, the combination of

115 *spectral and angular* information shows best performance *throughout the lower troposphere*

116 when the four most opaque frequencies are used with their angular information and the three

117 more transparent channels are added with their zenith measurement only. Note no significant

118 accuracy improvement is achieved for the retrieval of humidity profiles by adding elevation

119 scanning in Band A from ground based MWP.

120 Microwave radiometer observations during LAUNCH were taken at Falkenberg starting on,

121 0900 UTC 8 September 2005 and ended on 0700 UTC 1 November 2005. Unfortunately, on

122 1800 UTC 17 September 2005 the GPS clock failed which led to an omission of relative

123 calibrations until this was corrected for on 1200 UTC 17 October 2005. Because the data in

124 this time interval are of poor quality they are ignored in the following. HATPRO was

125 operated in a dual zenith/elevation-scanning mode: The elevation scans were carried out every

126   20 min and lasted about 5 min each with an integration time of 30 s at each angle. These

127   measurements provide the base for very accurate temperature profiles in the lower BL. In

128   between the elevation scans, zenith observations were carried out at a temporal resolution of

129   1s. Thus, in between the accurate temperature profile determination, optimal estimates of

130   humidity and LWC profiles are available on a high temporal resolution.

131   **2.2. Active Instrumentation**

132   The cloud radar data employed in this study was measured by the commercially available

133   instrument MIRA36 operated by the University of Karlsruhe and built by METEK GmbH

134   (http://www.metek.de/produkte.htm). It was stationed at the Falkenberg site from 16

135   September 2005 to 05 November 2005 only ~10 m away from HATPRO. MIRA36 is a pulsed

136   radar operating at 36 GHz with a maximum sensitivity of -44 dBZ at 5 km at 0.1 s integration

137   time. The vertical resolution used is 30 m up to a maximum height of 15 km. In this study the

138   measurements of the radar reflectivity factor (Z) and Doppler velocity (v_d) are used for target

139   classification and LWC profile retrieval.

140   The ceilometer deployed at Falkenberg during LAUNCH is a Vaisala LD40 of DWD with a

141   temporal resolution of 15 s. This instrument measures a backscatter profile which is used to

142   detect cloud base and to retrieve the extinction profile needed by K06. In this study for the

143   lidar extinction profiles estimation we have used the inversion algorithm according to Klett

144   (1981) that involves only one boundary value for the solution of the lidar equation: the

145   absolute extinction on some reference level, which should be as far away from the lidar as

146   possible. This method assumes a power-law relationship between range dependent lidar

147   backscattering coefficient and optical extinction, where the exponent is considered to be unity

148   for water clouds. (Rocadenbosch and Comeron, 1999 & Rogers et al, 1997). Lidar-

149   ceilometers are more sensitive to small cloud particles than cloud radars, which in turn are

150   highly sensitive to larger drops. Thus, lidar-ceilometer measurements are more accurate in

151   deriving the actual cloud base height while cloud radars often detect light drizzle with

152   negligible LWC below the actual cloud base. Also, often cloud radars are not sensitive

153   enough to detect small droplets occurring in developing cumulus, which are, however, usually

154   captured by lidar-ceilometers. Generally lidar-ceilometers cannot be used to detect the vertical

155   cloud structure because most liquid water clouds are optically thick in the optical region of

156   the spectrum such that the lidar-ceilometer signal will almost always be extinguished in the

157   lower part of the cloud.

158   **2.3. In-situ Measurements**

159   The Lindenberg site has one of the longest historical data records of aerological

160   measurements dating back to 1905. First height soundings were performed with kites reaching

161   altitudes of up to ~10 km (Neisser and Steinhagen, 2005). Still today, a research focus is on

162   vertical soundings of the atmosphere and thus radiosondes are launched 4 times daily at 0000,

163   0600, 1200 and 1800 UTC. Additionally, at the Falkenberg site, DWD maintains a 99 m mast

164   with continuous measurements of temperature and humidity taken at six levels (10, 20, 40, 60,

165   80 and 98 m) with an integration time of 10 min.

166   **3. Retrieval Method**

167   The true atmospheric state vector **x** - to be retrieved in this study - consists of vertical profiles

168   of atmospheric temperature (**T**), absolute humidity ($\boldsymbol{\rho_v}$) and cloud liquid water content

169   (**LWC**), such that we can notate **x**=(**T**, $\boldsymbol{\rho_v}$, $\log_{10}$(**LWC**)). From here on vectors will be noted

170   in bold (here i.e. profile vectors). We retrieve $\log_{10}$(**LWC**) instead of directly **LWC**, because

171   the distribution of $\log_{10}$(LWC) more closely resembles a Gaussian shape than LWC and

172   additionally, we do not have to worry about negative LWC values within the retrieval

173   procedure. Multiple liquid water cloud layers can also be retrieved and state no limitation to

174   the method. The vertical grid of T and ρ_v is set to 50 m in the lowest 200 m and then increases

175   gradually to 150 m at 1000 m, 250 m at 3000 m and 500 m at 10 km above the surface –

176   corresponding approximately to typical height grids in state-of-the-art NWP. LWC, however,

177   is retrieved on the vertical grid of the target classification.

3.1. Measurement Inversion

179   The goal of the IPT is to retrieve $\mathbf{x}$ by optimally exploiting the information from a given

180   measurement vector $\mathbf{y}$ (Rodgers, 2000). Depending on the situation, $\mathbf{y}$ will consist of a

181   specified vector of brightness temperatures $\mathbf{TB}$ and, in the cloudy cases, additionally of a

182   vector of radar reflectivities $\mathbf{Z}$, i.e. $\mathbf{y} = (\mathbf{TB}, \mathbf{Z})$. Principles of the method are described in

183   detail by L07 and L04; here we want to focus on the improvements made in the last years and

184   will thus only give a short method overview.

185   Generally in remote sensing applications, determining $\mathbf{x}$ from $\mathbf{y}$ directly is an

186   underdetermined and ill-conditioned problem, meaning that no unique solution exists and that

187   very small errors in the measurement may lead to huge deviations in the derived atmospheric

188   profile. A way to solve this problem is to add *a priori information*, i.e. information about the

189   atmospheric state which is given *prior* to the measurement, e.g. climatological information or

190   data from the closest radiosonde. Typically, the optimal estimation equations (e.g. Rodgers

191   2000) are used for combining measurement and a priori information. If the relationship

192   between $\mathbf{x}$ and $\mathbf{y}$ is slightly to moderately non-linear, an optimal atmospheric state $\mathbf{x}_{op}$ can be

193   found by iterating the following formulation

194   $$\mathbf{x}_{i+1} = \mathbf{x}_i + \left(\mathbf{K}_i^T \mathbf{S}_e^{-1} \mathbf{K}_i + \mathbf{S}_a^{-1} \right)^{-1} \times \left[\mathbf{K}_i^T \mathbf{S}_e^{-1} \left(\mathbf{y} - \mathbf{y}_i \right) + \mathbf{S}_a^{-1} \left(\mathbf{x}_a - \mathbf{x}_i \right) \right] \qquad (1)$$

195   where i represents the iteration step, $\mathbf{x}_a$ the a priori profiles of T, ρ_v and LWC, $\mathbf{S}_a$ the *a priori*

196   covariance matrix and $\mathbf{S}_e$ the combined measurement and forward model error covariance

197   matrix. $\mathbf{K}_i = \partial \mathbf{F}(\mathbf{x}_i) / \partial \mathbf{x}_i = \partial \mathbf{y}_i / \partial \mathbf{x}_i$ represents the so-called Jacobian, or the sensitivity of the

198   forward model to changes in $\mathbf{x}$, whereby $\mathbf{K}_i$ is re-calculated for each iteration. The forward

199   model $\mathbf{F}$ transforms from the state space ($\mathbf{x}$) to the measurement space ($\mathbf{y}$) in a straight-

200 forward way. E.g., given a space vector at a certain iteration $\mathbf{x}_i$, $\mathbf{F}$ calculates $\mathbf{TB}$ by applying

201 the Radiative Transfer Operator (RTO) at the HATPRO frequencies and, in the cloudy case

202 only, $\mathbf{Z}$ by assuming a specified Z-LWC power law relationship of the form $Z = a\ \mathrm{LWC}^b$.

203 Thus, the forward model can be noted in the following way:

$$\mathbf{F(x)} = \left\{ \begin{array}{c} \mathrm{RTO}(\mathbf{T,q,LWC}) \\ a \cdot \mathbf{LWC}^b \end{array} \right\} = \left\{ \begin{array}{c} \mathbf{TB} \\ \mathbf{Z} \end{array} \right\} = \mathbf{y} \qquad (2)$$

205 Optimally, the formulation of Eq. 1 should guarantee the minimization of a quadratic cost

206 function between $\mathbf{x}_a$ and $\mathbf{x}_i$, respectively $\mathbf{y}$ and $\mathbf{y}_i$, when the difference between $\mathbf{x}_{i+1}$ and $\mathbf{x}_i$ goes

207 towards zero. The iteration procedure is terminated after an optimal number of iterations

208 ($i=op$) when IPT has converged to a sensible point. Here a quadratic cost function is applied

209 to determine whether the retrieved $\mathbf{F(x}_{op})$ is adequately close to the $\mathbf{F(x}_{i-1})$ of the prior

210 iteration (for more on the convergence criterion see L04). It is important to note that the

211 solution $\mathbf{x}_{op}$ must be interpreted as the most probable solution of a Gaussian distributed

212 probability density function, whose covariance can be written as:

$$\mathbf{S}_{op} = \left(\mathbf{K}_i^T \mathbf{S}_e^{-1} \mathbf{K}_i + \mathbf{S}_a^{-1} \right)^{-1}. \qquad (3)$$

214 The diagonal elements of this matrix give an estimate of the mean quadratic error of $\mathbf{x}_{op}$,

215 whereas the off-diagonal elements yield information on the correlation of retrieval errors

216 between the different heights.

217 A further important measure for retrieval algorithm evaluation is the averaging kernel matrix $\mathbf{A}$

218 which states the sensitivity of the retrieved to the true state ($= \partial\mathbf{x}_{op}/\partial\mathbf{x}$). In the case of Gaussian

219 statistics, $\mathbf{A}$ can be written as

$$\mathbf{A} = \mathbf{S}_{op} \cdot \left(\mathbf{K}_i^T \mathbf{S}_e^{-1} \mathbf{K}_i \right). \qquad (4)$$

221   The diagonal values of **A** are frequently used as a measure of vertical resolution (Rodgers,

222   2000) whereas the trace of **A** states the independent number of levels which can be retrieved

223   from a given measurement.

224   **3.2. Target Classification**

225   The current IPT version described in this study is not applicable to atmospheric columns

226   containing significant precipitation as well as columns with ice and liquid phase occurring at

227   one level. In the first case problems with the instruments' performance occur (e.g. wet MWP

228   radome or radar attenuation effects), whereas in the latter case the radar cannot easily

229   distinguish the contributions of ice and liquid water to Z.

230   In order to identify regions where and where not the IPT can be applied, we have employed

231   the Cloudnet (Illingworth et. al, 2007) target classification scheme developed at the

232   University of Reading, UK. This scheme classifies the targets, which contribute to the

233   backscattered radiation received either by the cloud radar or the lidar ceilometer (Fig. 1). With

234   this classification scheme it is possible to discriminate if the backscattered radiation originates

235   e.g. from liquid clouds, ice clouds, precipitating or non-precipitating clouds or even aerosols

236   or insects. The radar and lidar observations are first averaged to a common grid (i.e. 30 s in

237   time and 60 m in height) and then supplemented by temperature, pressure, humidity and wind

238   speed from an operational NWP model to assist with attenuation correction and cloud phase

239   identification. The full details of how the backscatter targets in each radar/lidar pixel are then

240   categorized into a number of different classes are given by Hogan and O'Connor (2006), but

241   essentially we make use of the fact that radar is sensitive to large particles such as rain and

242   drizzle drops, ice particles and insects, while the lidar is sensitive to higher concentrations of

243   smaller particles such as cloud droplets and aerosol. We define drizzle as water droplets

244   greater than 50 μm in diameter, which have a significant fall terminal fall velocity. The

245   terminal fall velocity of the smaller cloud droplets (diameters less than 50 μm) is typically

246   only a few cm s^{-1}. Additionally, the high lidar backscatter of liquid droplets also enables

247   *super-cooled* liquid layers to be identified even when embedded within ice clouds (Hogan et

248   al. 2003).

3.3. Clear Sky Mode

250   If the target classification identifies a profile without any clouds or the detected cloud layers

251   consist of pure ice phase, the "clear-sky" mode is used to retrieve the atmospheric state vector

252    $\mathbf{x} = (\mathbf{T}, \boldsymbol{\rho}_v)$. Note that the employed microwave frequencies show no sensitivity to non-

253   precipitating ice clouds. To optimally exploit the capabilities of HATPRO concerning T-

254   profiling, the measurement vector consists not only of the 14 zenith-pointing TBs of all

255   HATPRO channels, but additionally of 20 TBs at five off-zenith elevation angles (θ=42.0,

256   30.0, 19.2, 10.2, 5.4) at the four HATPRO channels 11-14 (ν = 54.94, 56.66, 57.30, 58.00

257   GHz) adding up to a total of 34 TB values. Because the atmosphere is close to optically thick

258   at 55-58 GHz, the lower elevation angles add more information content on the lower part of

259   the atmospheric temperature profile than the higher elevation angles and vice versa. This

260   effect, together with the height resolution contained in the frequency dependent

261   measurements, leads to an enhanced vertical resolution of the BL temperature profile. The six

262   angles correspond to air mass factors of ~ 1, 1.5, 2, 3, 6 and 10 and were originally chosen in

263   order to optimize statistical retrievals of T-profiles (Crewell and Löhnert, 2007).

264   To practically rule out the possibility of HATPRO being influenced by a cloud at an off-

265   zenith elevation angle, the ceilometer time series of lowest cloud base at ±20 min around the

266   time of measurement is analyzed. In case there are no clouds detected within this time

267   interval, we assume the atmosphere is horizontally stratified. It must be mentioned, that in a

268   small percentage of cases, this assumption may be wrong due to persistent cloud structures

269   occurring at a fixed position relative to the measurement site. In future this uncertainty may

270   be accounted for by using a simultaneous scanning infrared radiometer. For the case that a

271 cloud is detected, the *lowest* cloud base detected in this period is compared to a threshold

272 value derived from a TB climatology (Tab. 1). This climatology is based on a 10-year

273 radiosonde data set of Lindenberg including the years 1996 – 2005 with operational launches

274 at 0000, 0600, 1200 and 1800 UTC. It contains simulated TBs at all elevation angles

275 calculated with (TB_{cloud}) and without liquid clouds (TB_{clear}). Liquid clouds have been placed

276 within the radiosonde ascent using a threshold value of 95% in humidity and a modified

277 adiabatic assumption (Karstens et al. 1994). For a given elevation angle-frequency

278 combination, the scatter of cloud base versus ΔTB (=$|TB_{cloud}-TB_{clear}|$) shows the influence of a

279 cloud at a certain height to the observed TB. Based on these statistics we determine a critical

280 cloud base threshold to include only those off-zenith TB observations (of the originally 20

281 off-zenith TB observations) in the retrieval where the lowest observed cloud base indicates a

282 ΔTB of less than 0.1 K (Tab. 1). In case of a clear sky observation in the zenith, but the

283 occurrence of a cloud base of lower than 69 m in the +-20 min time window around the zenith

284 observation, this would mean excluding the elevation angles 42°, 30°, 19° at 54.94 GHz.

285 Sensitivity studies showed that the temperature retrieval accuracy in this case is reduced no

286 more than 0.1 K throughout the profile in comparison to the case when using all angle-

287 frequency combinations.

288 For the retrievals applied to the elevation scans, the a priori profile $\mathbf{x}_a$ consists of the

289 temporally interpolated profiles of temperature and humidity using only the 0000 and 1200

290 UTC Lindenberg radiosonde ascents. The $\mathbf{S}_a$ matrix is then calculated by evaluating the

291 temporally interpolated profiles at 0600 and 1800 UTC against the actual 0600 and 1800 UTC

292 ascents Lindenberg ascents using the 10-year radiosonde climatology. Thus, the diagonal of

293 $\mathbf{S}_a$ will contain the variance of this difference and the off-diagonal components the

294 corresponding covariances. The larger the diagonal components, the less weight is given to $\mathbf{x}_a$

295 in the retrieval process and vice-versa.

296   Between two subsequent elevation scans only zenith TBs are available, so that the

297   measurement vector will only consist of 14 values. Due to the expected higher **T**-accuracy

298   from the elevation scan retrievals, **T** derived from the latest available elevation scan is taken

299   as the temperature a priori profile between two subsequent scans. For the temperature part, the

300   covariance matrix $\mathbf{S}_a$ is set to the error covariance matrix $\mathbf{S}_{op}$ (Eq. 3), which describes the

301   uncertainty of the retrieved profile. For $\boldsymbol{\rho}_v$ the a priori information is always taken from the

302   statistics of the temporally interpolated radiosonde profiles.

3.4. Cloudy Sky Mode – LWC calculation

304   The target classification scheme allows the identification of the liquid cloud regions within

305   the profile. If this is the case, the assumption of a horizontally stratified atmosphere is again

306   no longer given due to the strong variability connected with clouds. To still be able to make

307   use of the elevation scans, the same cloud base threshold method as described in section 3.3 is

308   applied. Also the a priori assumptions for **T** and $\boldsymbol{\rho}_v$ are identical to the ones applied to the

309   clear sky mode.

K06 Method for LWC profiling

312   In order to infer LWC from the radar reflectivity Z, a power law relationship $Z = a\,\mathrm{LWC}^b$ is

313   often used (e.g. Fox and Illingworth, 1997) with fitting parameters a and b. Typically, for

314   non-precipitating clouds, Rayleigh scattering conditions are given meaning that Z is equal to

315   the 6th moment of the drop size distribution (DSD). However this also means that a small

316   number of larger particles (i.e. drizzle) can contribute to the major part of the Z without a

317   strong contribution to the LWC and the effective radius. A typical Z-LWC diagram calculated

318   from DSD measured in-situ from aircraft during four field campaigns is presented in Fig. 2a.

319   It shows up to 40 dB variability in Z for a fixed value of LWC. Using the ratio Z/α between

320   the radar reflectivity Z and ceilometer optical extinction α as a discriminating parameter, K06

321   and Krasnov and Russchenberg (2002) have developed a technique, which discriminates

322　between 3 categories of water clouds – "without drizzle" (the drizzle fraction contribution to

323　radar reflectivity Z and LWC is negligible and the DSD can be described by a standard

324　modified gamma or log-normal three parameter distribution), "light drizzle" (the drizzle

325　fraction dominates Z, but its contribution to LWC is less then 0.03 g m^{-3}) and "heavy drizzle"

326　(Z is completely determined by the drizzle fraction and its contribution to LWC is significant,

327　whereby the DSD is characterized as a mixture of two independent distributions). For each

328　category a specific Z-LWC power law (i.e. different a, b coefficients) is derived (see Figs. 2b-

329　d and Tab. 2).

330　If the lidar signal within the cloud is attenuated and no radar-to-lidar ratio Z/α is available, Z

331　thresholds (-35 and -20 dBZ) are used to determine the water cloud category. These

332　thresholds are derived from simultaneous cloud measurements of radar and lidar with known

333　lidar optical extinction using the extensive Cloudnet database archive from the four European

334　sites Cabauw (NL), Chilbolton (UK), Palaiseau (F) and Lindenberg (D).

335　Once the water cloud category has been identified via Z/α or Z threshold, the appropriate

336　coefficients a and b are chosen and are then used within the forward model $\mathbf{F}$ (Eq. 2) to

337　calculate LWC within the retrieval procedure. The accuracy of each of the derived Z-LWC

338　relationships is also derived from the in-situ data of the four field campaigns shown in Fig. 2.

339　This is done by applying the derived Z-LWC relationship to the in-situ determined value of Z

340　and then calculating the mean square difference of the retrieved LWC to the actually

341　measured LWC. Hence, the corresponding diagonal components of $\mathbf{S}_e$ are determined.

342　*LWC a priori profile*

343

344　In contrast to L04, where a mean LWC profile derived from multiple singular column cloud

345　model runs is used as a priori, the LWC a priori profile used here is calculated using a

346　modified adiabatic approach (Karstens et al. 1994). The main advantage is that no restrictions

347　concerning cloud vertical extension as in L04 (maximum cloud extension of 1500 m) and

348 vertical resolution (formerly 250 m) apply. This approach is applied to all height levels

349 containing the cloud categories "without drizzle" and "light drizzle" from K06. Generally, the

350 liquid water content as calculated for an adiabatic ascent (LWC$_{ad}$), (e.g. Rogers and Yau

351 (1989)), is assumed to be the maximum possible LWC and is corrected for effects of dry air

352 entrainment, freezing drops or precipitation in the modified adiabatic approach. The empirical

353 correction function used was derived from aircraft measurements of LWC in different types

354 of non-precipitating clouds (Warner 1955)

355 $$\text{LWC} = \text{LWC}_{ad}\left(1.239 - 0.145\ln(h)\right) \qquad (5)$$

356 with h in m indicating the height above cloud base and h within the range between 1 m and

357 5140 m.

358 As a further constraint to minimize the degrees of freedom, the humidity is set to its saturation

359 value within the detected cloud boundaries. The saturation value of ρ_v in a specific cloud layer

360 is determined using the corresponding T value of the prior iteration. For the first iteration, the

361 first guess value of T is used.

362 **4. IPT Application to simulated cases**

363 In this section we would like to show the accuracy improvements achieved by including the

364 elevations scans for the retrieval of temperature profiles. This is done on the basis of a

365 simulation study for clear sky situations when the strongest temperature variations are

366 expected due to strong radiative fluxes at the surface. Löhnert et al. (2007) have performed an

367 extensive accuracy assessment of the IPT within a NWP model domain using zenith

368 measurements only, so this will not be the main focus of this section. Here radiosonde ascents

369 from Lindenberg identified as "clear sky" of the years 1997 and 2002 (in total 1130 ascents)

370 are used to calculate the 34 HATPRO TBs (section 3.3) needed for boundary layer profiling

371 for each radiosonde ascent. Here, we use a radiative transfer model according to Czekala and

372   Simmer (2002) together with a Fast Absorption Predictor (FAP) based on the absorption

373   model by Rosenkranz (1998) to calculate the absorption coefficients of the relevant gaseous

374   components (oxygen, water vapour and nitrogen) in the microwave region (for more details

375   on FAP see L04). The absorption coefficient for liquid water is calculated in a straight

376   forward way using the model according to Liebe (1993). A channel dependent Gaussian noise

377   factor to account for radiometric noise and random calibration uncertainty is added to the

378   simulated TBs on the basis of HATPRO clear sky observation during periods of low

379   variations in total atmospheric water vapour amount (IWV). On this basis the channels 1 − 7

380   are assigned with a noise factor of 0.4 K, channels 8 − 10 with 0.5 K and channels 11 − 14

381   (including the elevation scans) with 0.2 K. During an elevation scan, the uncertainties of the

382   measurements at one and the same frequency but at different elevation angles are probably

383   not independent. Currently we have not included this fact in the calculation of the $\mathbf{S}_e$ matrix −

384   the instrument uncertainties are only included in the diagonal components of $\mathbf{S}_e$. This may

385   have small influence on the error characteristics or even the vertical resolution of the retrieval

386   results.

387   In order to evaluate the IPT performance, the retrieved $\mathbf{T}$ is compared to the true $\mathbf{T}$ profile,

388   but also to the a priori profile, which consists of the temporally interpolated radiosonde

389   profile (section 3.3). Thus, the comparisons show us which accuracy is gained by adding the

390   HATPRO measurements to the a priori information. Results are shown for two IPT runs: one

391   using all 34 TBs, including the elevation scans of the channels 11, 12, 13 and 14 (IPT_ELE)

392   and the other using the 14 zenith observed TBs only (IPT_ZEN). Note that the channels 1 − 7

393   are used in both retrievals because the humidity profile is retrieved simultaneously to the

394   temperature profile. Compared to the a priori profile, the increase in (Root Mean Square)

395   RMS accuracy is the most pronounced near the surface and decreases to the order of 0.1 K

396   above 2 km height (Fig. 3a) for both IPT_ZEN and IPT_ELE. Above this height the

397   information added to the retrieval by remote sensing is nearly zero. Close to the surface a

398 slight negative BIAS in the temperature a priori profile occurs which can be compensated

399 both by IPT_ZEN und IPT_ELE. IPT_ELE shows RMS accuracies as low as 0.3 K close to

400 ground and lower than 1 K in the lowest 3 km. In the lowest 2 km the average RMS accuracy

401 of IPT_ZEN is 0.85 K and of IPT_ELE 0.59 K, whereas the a priori profile shows an

402 accuracy of 1.43 K. IPT_ELE outperforms IPT_ZEN on average by 0.26 K in the lowest 2

403 km. Above this height the influence of the elevation scans is no longer significant.

404 Starting from the a priori estimate for the actual humidity profile (RMS accuracies are less

405 than 1.1 gm^{-3} throughout the profile), both IPT versions enhance the average RMS accuracy

406 in the lowest 5 km from 0.77 to 0.60 gm^{-3} (Fig 3b). The influence of the remote sensing

407 observations extends to higher levels than in the temperature case due to the fact, that the

408 humidity weighting functions of the Band A channels are approximately constant with height.

409 Note that, as expected, no significant differences are observed between IPT_ZEN and

410 IPT_ELE in case of the humidity retrieval.

411 The increase in temperature RMS accuracy below 1 km is especially relevant for resolving

412 boundary layer inversions (BLI). To evaluate the BLI cases, we have analyzed all profiles

413 containing a temperature increase with height over layers of at least 100 m (667 out of 1130

414 cases). As shown by a typical near-surface BLI example, IPT_ELE reproduces **T** much more

415 realistically than IPT_ZEN (Fig. 4a). The average RMS accuracy of IPT_ZEN is 0.95 K and

416 of IPT_ELE 0.59 K for all BLI cases in the lowest kilometer above the ground (Fig. 4b). In

417 comparison to all analyzed cases, the accuracy of IPT_ZEN decreases, whereas the IPT_ELE

418 accuracy stays constant, underlining the strength of IPT_ELE in retrieving BLIs.

419 The T-retrieval performance of IPT_ELE in contrast to IPT_ZEN can also be regarded in

420 terms of number of independently retrievable layers. Generally IPT_ELE shows a higher

421 ability to resolve T perturbations with the number of independent levels of IPT_ELE and

422 IPT_ZEN being 3.3, respectively 1.7 (=tr(**A**), see Eq. 4). This underlines the need for

423   including elevation scans into microwave profiler retrievals of **T**. For the humidity retrieval,

424   the number of independent layers is dependent on the total water vapour amount in the

425   atmosphere, whereby the numbers range from 1.2 (low IWV) to 1.5 (high IWV).

5. Evaluation of IPT retrievals during LAUNCH

427   The IPT_ELE, as described in the sections above, has been continuously applied to the

428   measurements gathered at the Falkenberg remote sensing site during LAUNCH. In this

429   application we retrieve **T**, $\boldsymbol{\rho}_v$ and **LWC** by employing the method as described in section 3.4.

430   The retrievals are derived for 19 October 2005 − 31 October 2005, which was the only time

431   period when all the required instruments (i.e. microwave profiler, cloud radar and ceilometer)

432   were measuring simultaneously and without error. In total 7324 thermodynamic profiles have

433   been calculated. The first two days of the period were characterized mostly by dry weather,

434   with occasionally scattered low level liquid clouds and some cirrus aloft. During 21 October −

435   25 October frequent rain events dominate, with convective activity reaching up to 11-12 km

436   (21st, 25th) or long-lasting stratiform events (24th). During these periods IPT is not applicable

437   due to water on the radome of the microwave profiler leading to measurements that are not

438   interpretable. The last 6 days of the period are then characterized by a rather stable high

439   pressure period with some scattered BL cumulus on the 26th and 27th and no BL clouds from

440   the 28th to the 31st.

5.1. Comparison with mast observations

442   The mast measurements of T and ρ_v at the Falkenberg site, which are averaged on a 10 min

443   temporal grid, present an excellent possibility of evaluating the IPT results in the lowest 100

444   m. The obtained results from 19 October − 31 October are shown in Fig. 5, each evaluated at

445   50 m and 100 m above ground, which correspond to two of the three lowest levels in the IPT

446   vertical grid. For the 100 m comparison, the highest mast measurement (98 m) was used,

447   whereas the 50 m value was obtained by averaging the 40 and 60 m mast values. The RMS

448   differences between mast and IPT are very satisfactory and on the order of 0.5 − 0.6 K, with

449   negligible BIAS errors. Considering the random error of the mast measurements (~0.1 K) as

450   well as retrieval errors due to horizontal variations in the temperature field (~0.2 K), these

451   results agree very well with the predicted errors from the simulation experiment state

452   applying elevation scans. Since these simulation results were significantly lower than the IPT

453   errors resulting from the zenith-only mode (section 4), we conclude that the real

454   measurements also significantly benefit from the elevation scan procedure. It must be

455   mentioned, that these satisfactory retrieval results in the lower BL are largely due to the

456   capability of moving the elevation scan down 10.2° and even 5.4° above the horizon. This

457   was only possible due to the very flat terrain surrounding the Falkenberg measurement site.

458   Compared to the retrieval of T, the IPT performance with respect to ρ_v is not as convincing

459   (Fig. 5), mainly due to the fact that the height resolution is much poorer (section 4). The RMS

460   differences between mast and IPT are of the order of 0.8 gm^{-3}. These RMS values are slightly

461   (0.1 - 0.2 gm^{-3}) larger than the expected values from the simulation and additionally BIAS

462   errors on the order of 0.5 gm^{-3} occur. Next to horizontal humidity variations and random error

463   of the mast measurements, we expect unaccounted systematic calibration uncertainties of the

464   tower sensor and microwave profiler itself, as well as unknown errors of the microwave

465   absorption model to be causing these errors.

466   **5.2. Analysis of temperature time series**

467   In this section we analyze the IPT derived temperature time series in comparison to the

468   radiosonde and the LME model output (Figs. 6 and 7). Particularly, temporally highly

469   resolved developments of lowest boundary layer (0-500 m) are well represented in the IPT

470   (Fig. 6b), whereas these developments are naturally not detectable in the interpolated 12-

471   hourly radiosonde time series (Fig. 6a). For example, the strength of the stable nocturnal BL

472　inversion on the clear-sky days (19th, 27th-31st) is underestimated (Fig. 6f). The transition

473　from a stable to a well mixed BL is also not recoverable by using the 12-hourly interpolated

474　radiosonde profiles. This is expressed during daytime by the high positive deviations in Fig.

475　6f. The overestimations of the radiosonde with respect to the IPT temperatures occurring

476　during the well mixed BL in 500 − 1000 m also indicate that the gradient of the temperature

477　profile is not strong enough (i.e. less than 1 K/100m through the BL). The vertical "stripe-

478　like" structures seen in Fig. 6f occurring mainly in 1 to 3 km height must still be examined

479　more closely in future. We assume them to origin from a combination of radiometric noise

480　and horizontal inhomogeneities. However, in order to check the possibility of real temporal

481　variations in the vertical temperature profile, we plan to assess Raman lidar and/or tethered

482　balloon measurements during future campaigns (e.g. COPS 2007, http://www.uni-

483　hohenheim.de/cops/) which will give us independent and continuous temperature

484　measurements aloft. With the available data, it is currently not possible to evaluate these

485　effects conclusively.

486　The above mentioned characteristics can also be identified when analyzing the mean diurnal

487　cycle of the five clear-sky days in (Fig. 7), where the interpolated radiosonde temperature

488　amplitude is not able to follow the retrieved amplitude of the 12-hourly sondes. Note that the

489　radiosonde and IPT match at ~1100 UTC and not at 1200 UTC due to fact that the

490　radiosondes are generally launched ~45 min before scheduled time in order to account for the

491　duration of the ascent. Fig. 7a and 7b also nicely show the correspondence between the mast

492　measurements and IPT, which could be expected from the results discussed in section 5.1.

493　*Potential for model evaluation*

494　The potential of an IPT like method to evaluate the performance of a numerical weather

495　prediction model is also shown in Figs. 6 and 7. A precise representation of the BL is

496　essential in state-of-the-art numerical weather forecast models for correctly modeling

497 convection, clouds and regional precipitation events. An evaluation of the performance of

498 such models in the BL is thus of extreme importance and cannot be carried out using twice-

499 daily operational radiosonde data as demonstrated above. A combination of instruments as

500 used by the IPT may prove very valuable when comparing long-term time series of

501 thermodynamic profiles with model output from NWP. Microwave profiler, cloud radar and

502 ceilometer together provide a unique combination for the simultaneous retrieval of

503 temperature, humidity and cloud liquid water profiles with the respective error bars.

504 To show the potential for NWP evaluation we have also analyzed temperature fields of the

505 Lokal Modell (LME) of the German Weather Service calculated for the LAUNCH campaign

506 in a 24h forecast mode, with model runs commencing at 0000 UTC. Comparisons of these

507 forecasts with the interpolated radiosonde and the IPT retrievals are shown in Fig. 6. As can

508 be seen in Fig. 6d, LME represents the development of the lowest boundary layer more

509 accurately than the interpolated radiosonde, i.e. its behavior is very similar to that of the IPT.

510 This characteristic can also be seen in the mean diurnal cycle of the lowest temperatures (Fig.

511 7 and the 50 and 100 m level). However, the comparison at the 50 m level also shows that the

512 model overestimates the lowest temperature of the stable nocturnal BL in the early morning

513 hours with ~ 1K, whereas the decay of the well mixed daytime BL is too quick and model

514 temperatures are ~1.5 K too low at the end of the day. At 400 m the model shows a more

515 uniform mean temperature cycle than the IPT, with the tendency of too low temperatures in

516 the morning and too high temperatures in the afternoon. Fig. 6 shows further interesting

517 phenomena which can be analyzed by comparing IPT – LME. E.g. before noon time on

518 October 31st the boundary layer inversion was almost overcome in the model, but not nearly

519 in the measurements. Also interesting are the discrepancies concerning the development of

520 the BL inversion at mid to end of the 27th, where LME overestimates T on the order of 3 K

521 from 500 to 1500 m (also visible in the RS comparison).

522 It must be mentioned that these comparisons only encompass 6 clear-sky days and should not

523 be interpreted in a representative way. However, we do want to underline the potential of an

524 IPT like procedure for evaluating NWP for future applications.

5.3. LWC profile retrieval

526 The mean profiles of LWC calculated are shown in Fig. 8 as a function of height above cloud

527 base. Fig. 8 shows the results for clouds with vertical extensions up to 400 m binned in 100 m

528 steps. Retrievable clouds with vertical extensions larger than 400 m are not shown in Fig. 8

529 due to their very seldom occurrence. Of the 7324 calculated profiles, 2391 profiles were

530 identified as cloudy. We show results of LWC derived with the IPT for cloudy cases

531 described in section 3.4 and compare them to the method according to K06. Note that K06 has

532 been incorporated into IPT, but results still differ due to the fact that the IPT results not only

533 rely on Z, but also on the LWC a priori profile and the MWP brightness temperatures.

534 The mean LWP difference between IPT and K06 is -1.4 gm^{-2} showing a relatively good

535 agreement with respect to a total mean IPT-LWP of ~36.9 gm^{-2}. However, the RMS

536 difference between both methods is ~45 g m^{-2} showing the need for a more extensive

537 evaluation of the LWC profiles. This is, however, a difficult task since the truth is not

538 available. L07 report a IPT-LWP RMS error of ~6 g m^{-2} using simulated data and additionally

539 this was achieved for non-precipitating clouds only. In order to finally assess the accuracy of

540 IPT and K06, studies employing cloud models with spectrally resolved cloud microphysics

541 must be carried out in future. The shapes of the mean IPT and K06 profiles are also

542 completely different for all four vertical extensions. This is mainly due to the fact that for the

543 cloud class "non-drizzling" and "light drizzle" the IPT procedure uses the modified adiabatic

544 profile assumption (see section 3.4) as a priori information, which shows an increasing LWC

545 with height above cloud base. For the cloud class "heavy drizzle" no a priori assumption for

546   the LWC profile is made because a cloud with significant drizzle is not necessarily expected

547   to show an adiabatic like behavior.

548   **6. Conclusions**

549   This study has demonstrated advances in profiling the vertical thermodynamic structure of the

550   boundary layer by extending the Integrated Profiling Technique of L04 with elevation scan

551   information from the MWP, a sophisticated target classification scheme and a radar-lidar

552   method (K06) to retrieve LWC also within drizzling clouds. Thus, the IPT is now suited for

553   accurately retrieving the development of boundary layer inversions together with a more

554   generally applicable retrieval of liquid clouds in the BL. The evaluation of long-term IPT time

555   series has a very high potential for the evaluation of NWP models but also for satellite

556   retrievals, e.g. DWD Lindenberg is currently planning a METOP evaluation with IPT

557   retrieval data and the Royal Dutch Meteorological Service is currently running the IPT at the

558   remote sensing site Cabauw, NL to perform model validation and climatological studies.

559   KNMI will also be running the Reading target classification scheme in a near real time mode

560   shortly, so that advanced thermodynamic profiles will be continuously available. In this

561   respect is must be mentioned, that the IPT can also be adapted to run in a "now-casting" mode

562   using the latest available radiosonde as a priori information as demonstrated by L07.

563   However, more comparative studies must be carried out in order to finally characterize IPT

564   performance, especially in heights above 1 km. Here T retrievals are especially sensitive to

565   the absolute calibration of the MWP but also rely strongly on the microwave absorption

566   model, where uncertainties in the O_2 line-coupling may account for retrieval errors

567   (Boukabara et al., 2005). In this context, the Cabauw site is ideally suited for future IPT

568   assessment: here KNMI operates a 35 GHz cloud radar, a HATPRO instrument and a

569   ceilometer. It also has a 200 m tower, which will allow an IPT assessment during various

570 weather regimes over long time intervals and the operational radiosonde site with two

571 launches per day is only 30 km away – allowing at least an evaluation of systematic error in T

572 and ρ_v retrievals. These studies will also help in investigating whether such measurements

573 have potential for routine assimilation in NWP models. In this context, it is very helpful that

574 the IPT resembles a 1D variational procedure, which also provides error estimates for every

575 profile retrieval.

576 Future expansions of the IPT will consist of including measurements from infrared sensors

577 (e.g. a radiometer in the 9-12 micrometer range or a highly spectrally resolving Atmospheric

578 Emitted Radiance Interferometer - AERI). The retrievals will then also be made physically

579 consistent with the infrared radiances leading to more accurate retrievals of low water content

580 (< 30 gm^{-2}) liquid clouds, which are momentarily difficult to detect with HATPRO, but still

581 have a large impact on the solar radiation balance.

582

583

584

585

586

587

588

589

590

591 **Acknowledgements**

604

605

605 **References**

606 Atlas, D., 1954: The estimation of cloud content by radar. *J. Meteor.*, **11**, 309-317.

607 Baedi, R. J. P., J. J. M. de Wit, H. W. J. Russchenberg, J. S. Erkelens, and J. P. V. Poiares Baptista,

608   2000: Estimating Effective Radius and Liquid Water Content from Radar and Lidar Based on the

609   CLARE'98 Data-Set. *Phys. Chem. Earth (B)*, **25**, 1057-1062.

610 Boukabara, S., S.A. Clough, J. Moncet, A.F. Krupnov. M.Y. Tretyakov and V.V. Parshin:

611   Uncertainties in the Temperature Dependence of the Line-Coupling Parameters of the Microwave

612   Oxygen Band: Impact Study, 2005: *IEEE Trans. Geosci. Remote Sensing*, **43**, No. 5

613 Czekala, H. and C. Simmer, 2002: On precipitation induced polarization of microwave

614   radiation measured from space. *Meteorol. Z.*, **11**, 49–60

615 Crewell, S., and U. Löhnert, 2007: Accuracy of boundary layer temperature profiles retrieved

616   with multi-frequency, multi-angle microwave radiometry. *IEEE Trans. Geosci.*

617   *Remote Sensing*, in press.

618 Fox, N. I., and A. Illingworth, 1997: The potential of a spaceborne cloud radar for the

619   detection of stratocumulus. *J. Appl. Meteor.*, **36**, 676-687.

620 Hogan, R. J., and E. J. O'Connor, 2006: Facilitating cloud radar and lidar algorithms: the

621   Cloudnet Instrument Synergy/Target Categorization product. Cloudnet

622   documentation: *http://www.cloud-net.org/data/products/categorize.html*.

623 Hogan, R. J., A. J. Illingworth, E. J. O'Connor, and J. P. V. Poiares Baptista, 2003:

624   Characteristics of mixed-phase clouds: Part II: A climatology from ground-based

625   lidar. *Quart. J. Roy. Meteorol. Soc.*, **129**, 2117-2134.

626 Illingworth, A. J., R. J. Hogan, E. J. O Connor, D. Bouniol, M. E. Brooks, J. Delanoë, P.

627   Donovan, J. D. Eastment, N. Gaussiat, J. W. F. Goddard, M. Haeffelin, H. Klein

628   Baltink, O. A. Krasnov, J. Pelon, J.-M. Piriou, A. Protat, H. W. J. Russchenberg, A.

629   Seifert, A. M. Tompkins, G.-J. van Zadelhoff, F. Vinit, U. Willén, D. R. Wilson, and

630   C. L. Wrench, 2007: CLOUDNET Continuous evaluation of cloud profiles in seven

631   operational models using ground-based observations. *Bull. Amer. Meteor. Sci.*, in

632   press

633   Kadygrov E. N., and D. R. Pick, 1998: The potential performance of an angular scanning

634   single channel microwave radiometer and some comparisons with in situ observations,

635   *Meteorological Applications,* **5**, 393-404

636   Karstens, U., C. Simmer, and E. Ruprecht, 1994: Remote sensing of cloud liquid water,

637   *Meteorol. Atmos. Phys.*, **54**, 157-171

638   Klett, J. D., 1981: Stable analytical inversion solution for processing lidar returns. *Appl. Opt.*,

639   **17**, 211-220.

640   Krasnov, O. A., and H. W. J. Russchenberg, 2002: The relation between the radar to lidar

641   ratio and the effective radius of droplets in water clouds: an analysis of statistical

642   models and observed drop size distributions. *The 11th Conference on Cloud Physics*,

643   June 2-7, 2002, Ogden, UT, AMS.

644   Krasnov, O. A., and Russchenberg, H., 2006: A synergetic radar-lidar technique for the LWC

645   retrieval in water clouds. *7th International Symposium on Tropospheric Profiling*,

646   Boulder, Colorado, USA, June 11-17, 2006

647   Liebe, H. J., G. A. Hufford, and M. G. Cotton, 1993: Propagation modelling of moist air and

648   suspended water/ice particles at frequencies below 1000 GHz. *Atmospheric

649   Propagation Effects through Natural and Man-Made Obscurants for Visible through

650   MM-Wave Radiation*. AGARD-CP-542, 3.1-3.10.

651 Löhnert, U., E. van Meijgaard, H. Klein Baltink, S. Groß, and R. Boers, 2007: Accuracy

652 assessment of an integrated profiling technique for operationally deriving profiles of

653 temperature, humidity and cloud liquid water. *J. Geophys. Res.*, **112**, D04205,

654 doi:10.1029/2006JD007379

655 Löhnert, U., S. Crewell, and C. Simmer, 2004: An integrated approach towards retrieving

656 physically consistent profiles of temperature, humidity, and cloud liquid water. *J.

657 Appl. Meteor.*, **43**, 1295-1307

658 Löhnert, U., and S. Crewell, 2003: Accuracy of cloud liquid water path from ground-based

659 microwave radiometry, Part I: Dependency of cloud model statistics. *Radio Sci.*, **38**,

660 8041, doi:10.1029/2002RS002654.

661 Neisser, J, and H. Steinhagen, 2005: Die Historie des MOL 1905–2005, *Promet*, **31**, Nr. 2–4,

662 available from *http://www.dmg-ev.de/gesellschaft/publikationen/pdf/promet*

663 Rocadenbosch, F. and A. Comeron, 1999: Error Analysis for the Lidar Backward Inversion

664 Algorithm. *Appl. Opt*, **38**, 4461-4474

665 Rodgers, C. D., 2000: *Inverse methods for atmospheric sounding: Theory and practice*.

666 World Scientific, 238 pp.

667 Rogers, R. R., M.-F. Lamoureux, L. R. Bissonnette, R. M. Peters, 1997: Quantitative

668 Interpretation of Laser Ceilometer Intensity Profiles. *J. Atmos. Oceanic Technol.*, **14**,

669 396 - 411

670 Rogers, R. R., and M. K. Yau, 1989: A short course in cloud physics, Butterworth-

671 Heinemann, Woburn, MA, USA, 290 pp

672 Rose, T., S. Crewell, U. Löhnert, and C. Simmer, 2005: A network suitable microwave

673 radiometer for operational monitoring of the cloudy atmosphere. *Atmos. Res.*, Special

674   issue: CLIWA-NET: Observation and Modelling of Liquid Water Clouds, **75**, 183-

675   200, doi:10.1016/j.atmosres.2004.12.005.

676 Rosenkranz, P. W., 1998: Water vapour microwave continuum absorption: A comparison of

677   measurements and models. *Radio Sci.*, **33**, 919–928.

678 Warner, J., 1955: The water content of cumuliform clouds. *Tellus,* **7**, 449-457.

679

679   **Figure Captions**

680   **Fig. 1**: An example 24-hour time series of the target classification scheme (Lindenberg, 22

681   October 2005) according to Hogan and O'Connor (2006). A target classification index is

682   given below.

683   **Fig. 2**: Two-dimensional diagrams of the Z-LWC relation derived from in-situ aircraft data

684   from four different field campaigns (see also Tab. 2); (a) – all analysed datasets, (b) – for the

685   cloud "without drizzle" (F), (c) – for the cloud "light drizzle" (B), and (d) – for the cloud

686   "heavy drizzle" (K). The categorization has been carried using the radar reflectivity to lidar

687   optical extinction ratio: (b) $\log_{10}(Z/\alpha)$ < -1; (c) -1 < $\log_{10}(Z/\alpha)$< 1.8; and (d)

688    $\log_{10}(Z/\alpha)$> 1.8 (according to K06). In (b)-(d) the dashed line represents the derived Z-

689   LWC relationship, the bold line the average Z value for a given LWC and the dotted line the

690   corresponding standard deviation.

691   **Fig. 3**: Temperature (3a, left) and humidity (3b, right) BIAS and RMS errors for IPT

692   application to simulated radiances from 1130 clear-sky radiances. The dashed (IPT_ZEN)

693   and dashed-dotted (IPT_ELE) show the results using only zenith TB observations,

694   respectively zenith and elevation scanning observations. Additionally shown are the errors

695   of the a priori profile, which states the linear interpolation between two 12-hourly

696   radiosondes. Note that in the humidity plot IPT_ZEN and IPT_ELE cannot be differentiated

697   because they show nearly the same values.

698   **Fig. 4**: (a, left): Performance of IPT_ELE and IPT_ZEN in a strong low-level inversion case

699   compared to the radiosonde (RS). (b, right): BIAS and RMS errors of IPT_ZEN and

700   IPT_ELE applied to all the simulated data (Fig. 3) showing boundary layer inversion.

701   **Fig. 5**: Comparisons of IPT and mast measurements of temperature (top) and humidity

702   (bottom) at levels 50 and 100 m above ground.

703   **Fig. 6**: Time series of temperature and cloud base (black dots) in the lowest 3 km between

704   19 October and 31 October 2005. (a): interpolated radiosonde profiles (12 hourly), (b):

705   retrieved IPT profiles, (c): LME model profiles. Also: Time series of temperature difference

706 (d): interpolated radiosonde – LME profiles (e): IPT – LME profiles, (f): IPT – interpolated

707 radiosonde profiles. Radiosonde ascent times are marked "x". The vertical white bands

708 denote times when the IPT could not be applied, mostly due to missing data of one of the

709 instruments, precipitation, not fulfilled convergence criteria or radiometer calibration.

710 **Fig. 7**: Mean diurnal cycle of temperature derived during the 5 practically cloud-free days

711 27-31 October 2005 during LAUNCH for the different measurement-types IPT, radiosonde

712 (RS) and mast in comparison to the 24-h LME forecasts initialized at 0000 UTC. Results at

713 400 m do not include any mast measurements

714

715

716

717

718

719

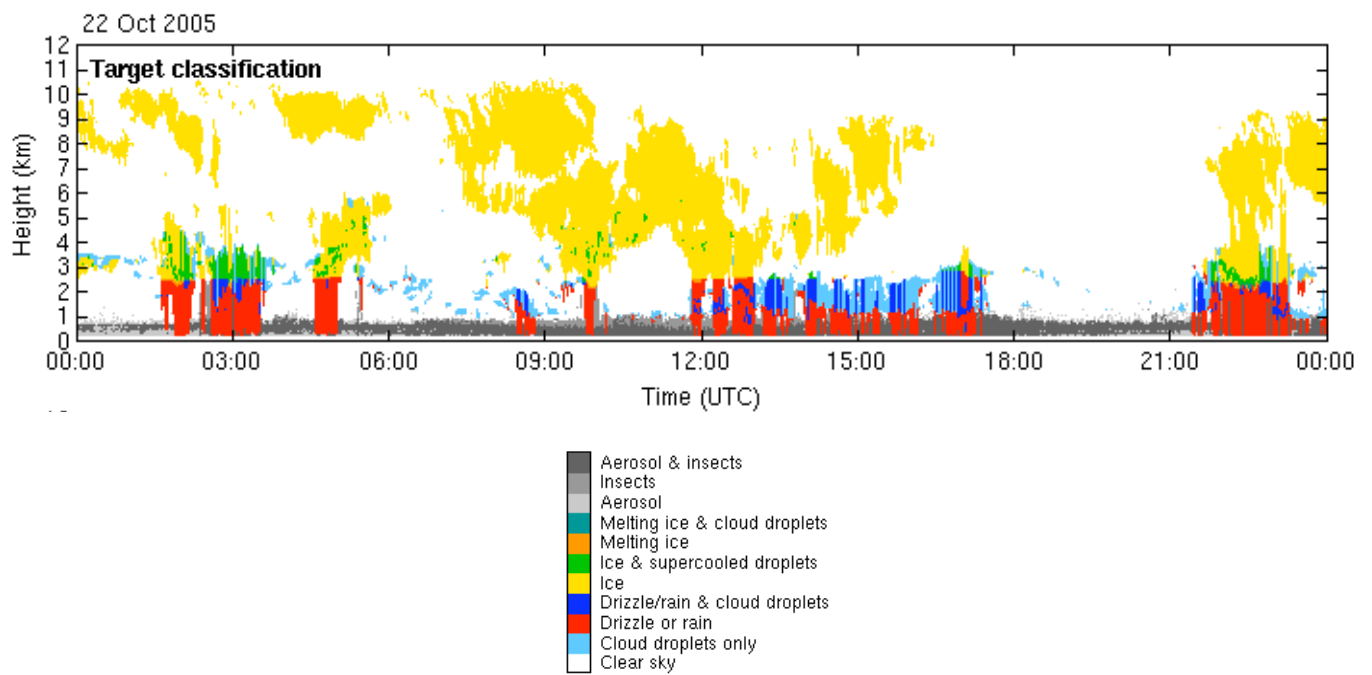720

721

722

723

724

725

726

727

728

729

730

731 **Figures:**

22 Oct 2005

Target classification

Aerosol & insects
Insects
Aerosol
Melting ice & cloud droplets
Melting ice
Ice & supercooled droplets
Ice
Drizzle/rain & cloud droplets
Drizzle or rain
Cloud droplets only
Clear sky

Fig. 1: An example 24-hour time series of the target classification scheme (Lindenberg, 22 October 2005) according to Hogan and O'Connor (2006). A target classification index is given below.
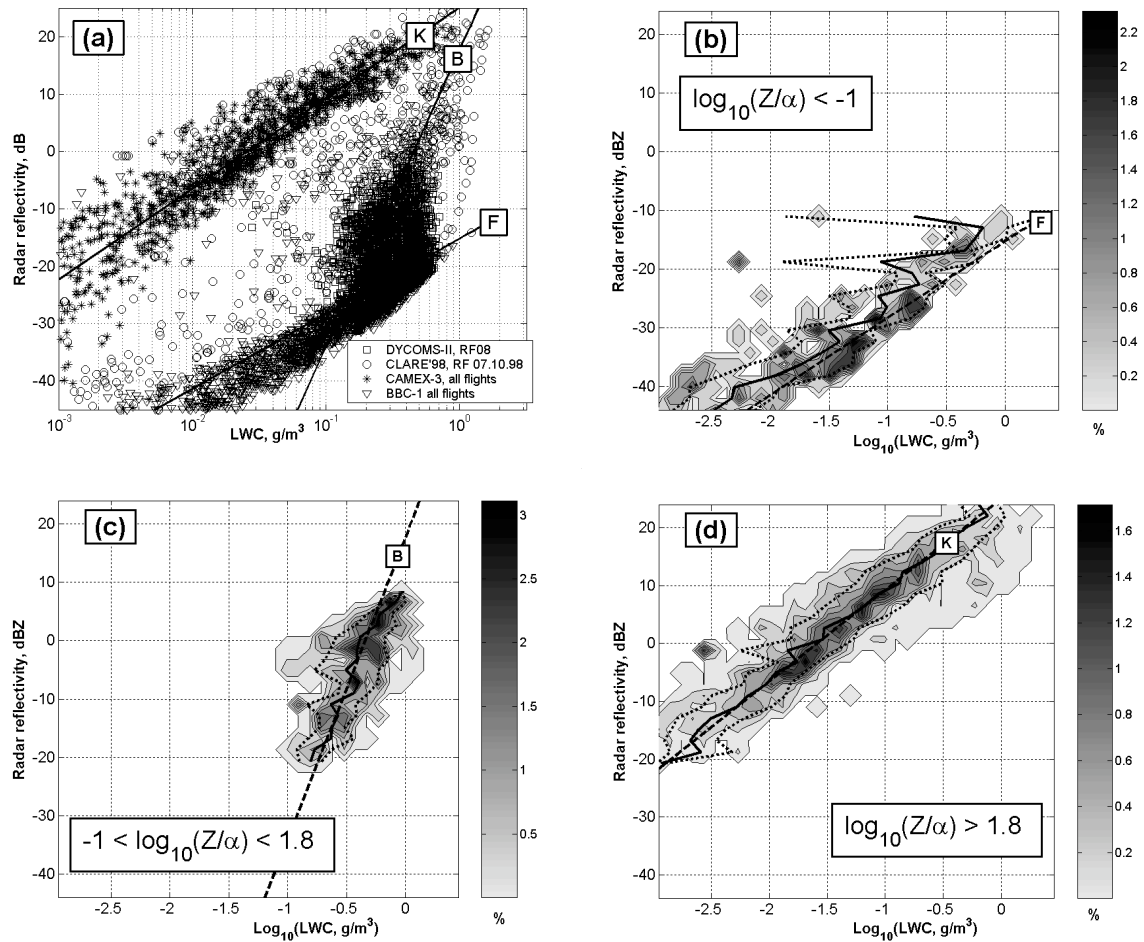
732

733

734

735

736

737

738

Fig. 2: Two-dimensional diagrams of the Z-LWC relation derived from in-situ aircraft data from four different field campaigns (see also Tab. 2); (a) – all analysed datasets, (b) – for the cloud "without drizzle" (F), (c) – for the cloud "light drizzle" (B), and (d) – for the cloud "heavy drizzle" (K). The categorization has been carried using the radar reflectivity to lidar optical extinction ratio: (b) $\log_{10}(Z/\alpha)$ < -1; (c) -1 < $\log_{10}(Z/\alpha)$ < 1.8; and (d) $\log_{10}(Z/\alpha)$ > 1.8 (according to K06). In (b)-(d) the dashed line represents the derived Z-LWC relationship, the bold line the average Z value for a given LWC and the dotted line the corresponding standard deviation.
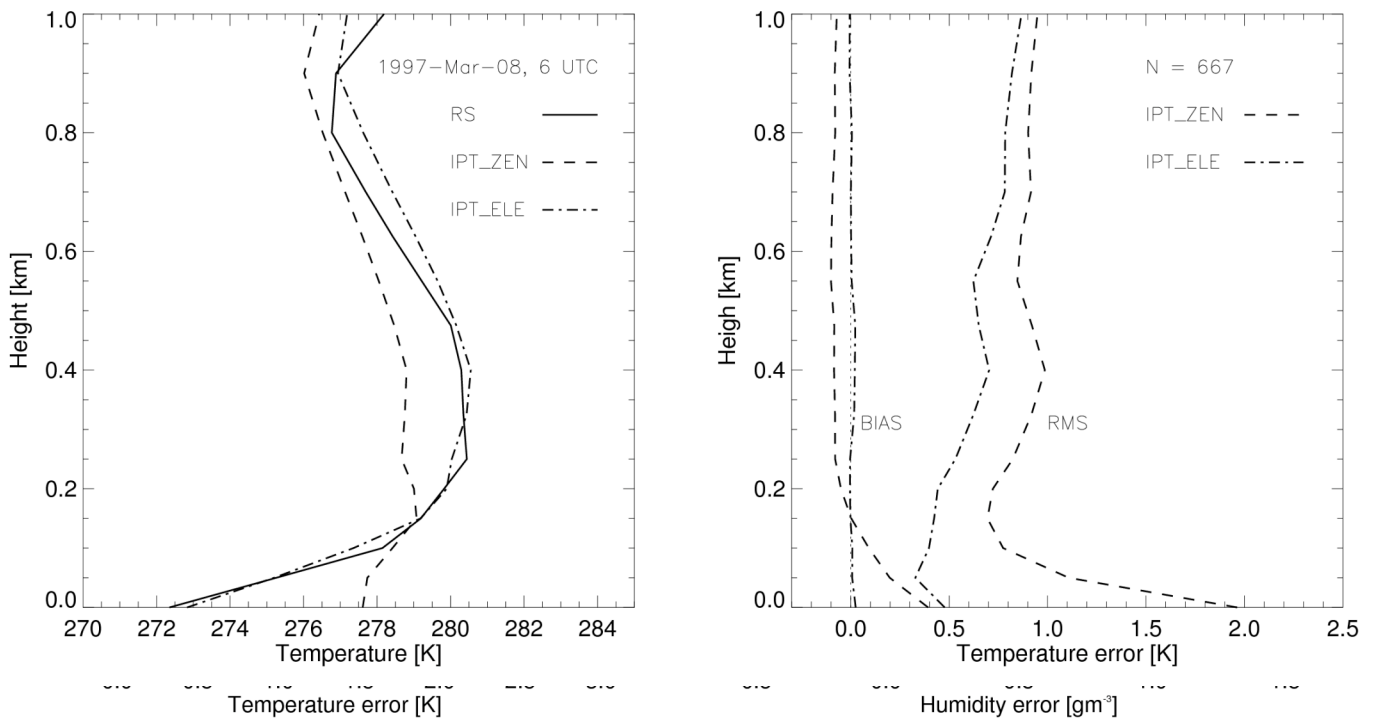
75

Fig. 4: (a, left): Performance of IPT_ELE and IPT_ZEN in a strong low-level inversion case compared to **Fig. 3**: Temperature (3a, left) and humidity (3b, right) BIAS and RMS errors for IPT application to the radiosonde (RS). (b, right): BIAS and RMS errors of IPT_ZEN and IPT_ELE applied to all the simulated radiances from 1130 clear-sky radiances. The dashed (IPT_ZEN) and dashed-dotted simulated data (Fig. 3) showing boundary layer inversion. (IPT_ELE) show the results using only zenith TB observations, respectively zenith and elevation

scanning observations. Additionally shown are the errors of the a priori profile, which states the linear

interpolation between two 12-hourly radiosondes. Note that in the humidity plot IPT_ZEN and

IPT_ELE cannot be differentiated because they show nearly the same values.
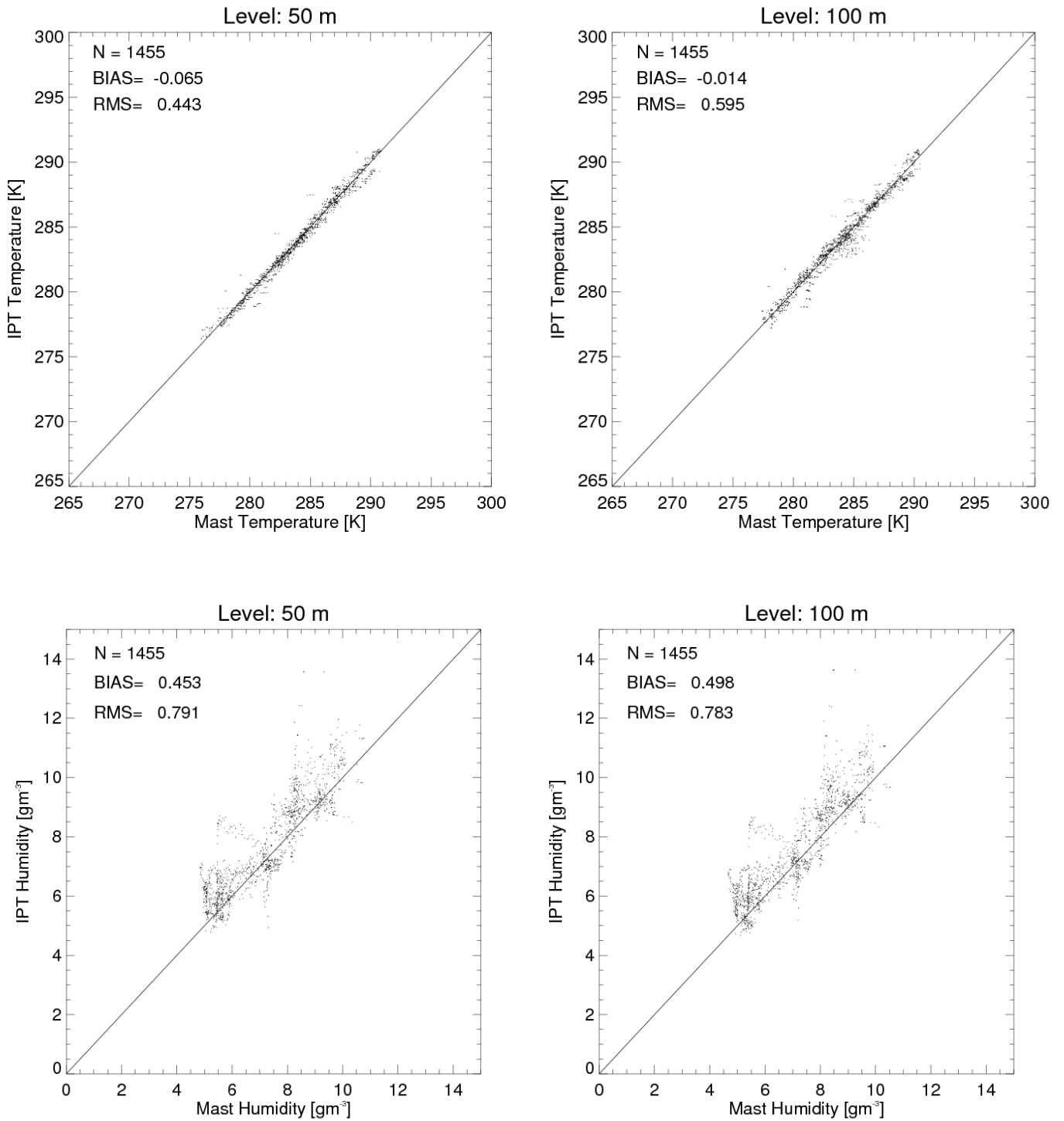
753

754

755

756

Fig. 5: Comparisons of IPT and mast measurements of temperature (top) and humidity (bottom) at levels 50 and 100 m above ground.
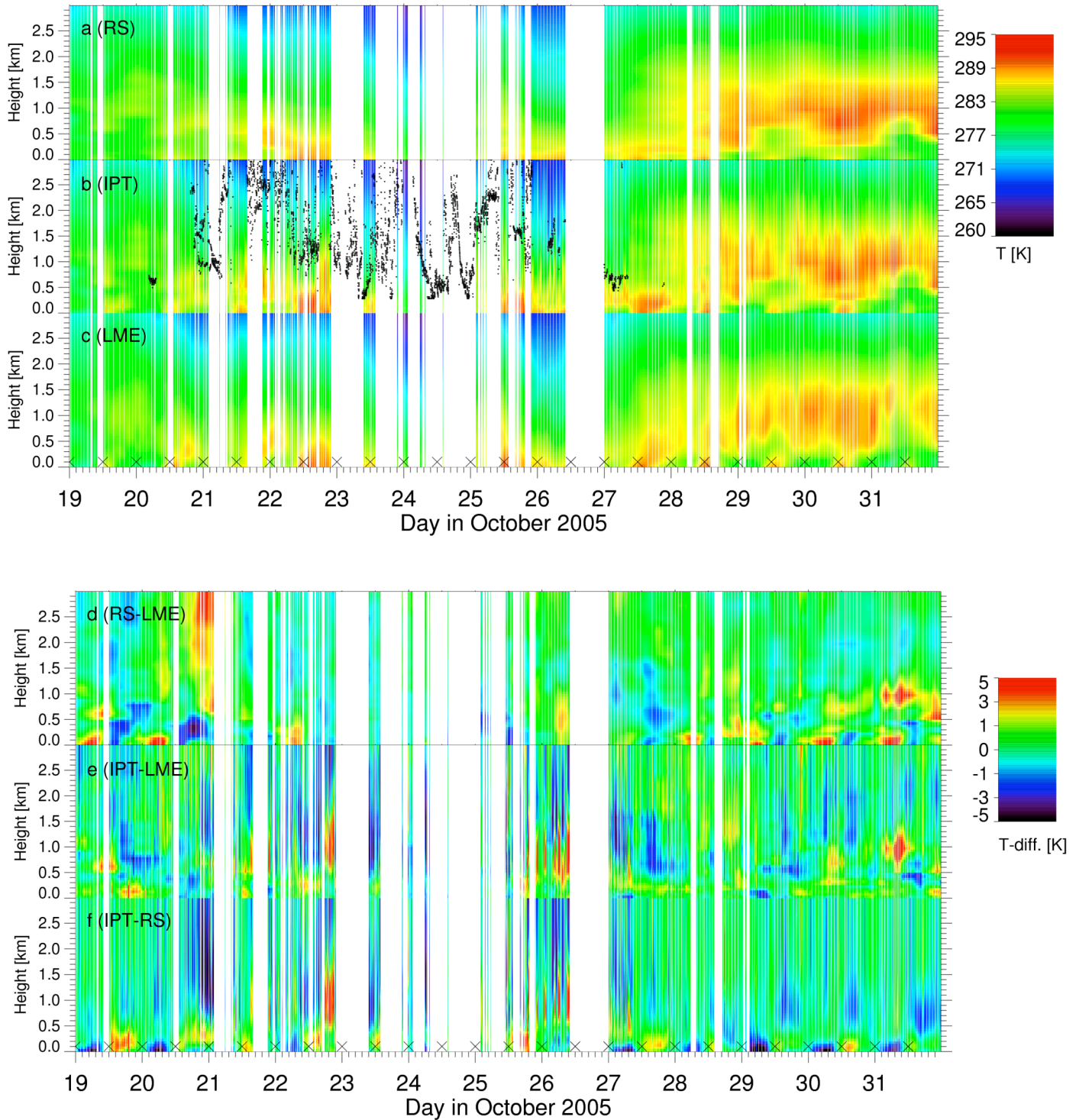
757

758

Fig. 6: Time series of temperature and cloud base (black dots) in the lowest 3 km between 19 October 2005 and 31 October 2005. (a): interpolated radiosonde profiles (12 hourly), (b): retrieved IPT profiles, (c): LME model profiles. Also: Time series of temperature difference (d): interpolated radiosonde – LME profiles (e): IPT – LME profiles, (f): IPT – interpolated radiosonde profiles. Radiosonde ascent times are marked "x". The vertical white bands denote times when the IPT could not be applied, mostly due to missing data of one of the instruments, precipitation, not fulfilled convergence criteria or radiometer calibration.
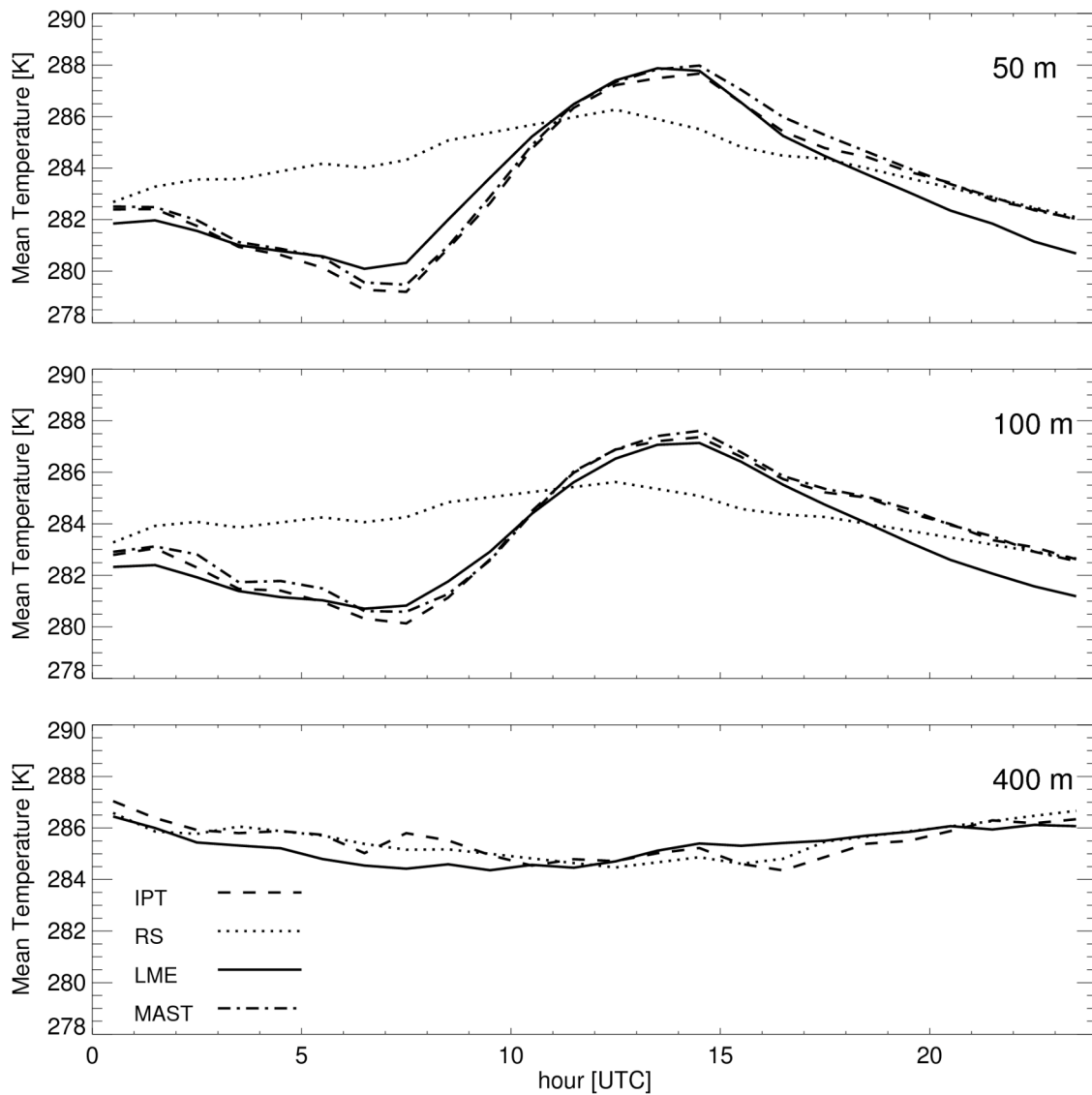
Fig. 7: Mean diurnal cycle of temperature derived during the 5 practically cloud-free days 27-31 October 2005 during LAUNCH for the different measurement-types IPT, radiosonde (RS) and mast in comparison to the 24-h LME forecasts initialized at 0000 UTC. Results at 400 m do not include any mast measurements

759

760

761

762

763

Tab. 1: Critical cloud base height in m for boundary layer profiling. Cloud bases higher than the critical cloud base have an influence of less than 0.1 K on TB(θ, ν). The abbreviation "**n.i.**" (= no influence) indicates that no clouds were detected that had an influence of more the 0.1 K on TB(θ, ν).

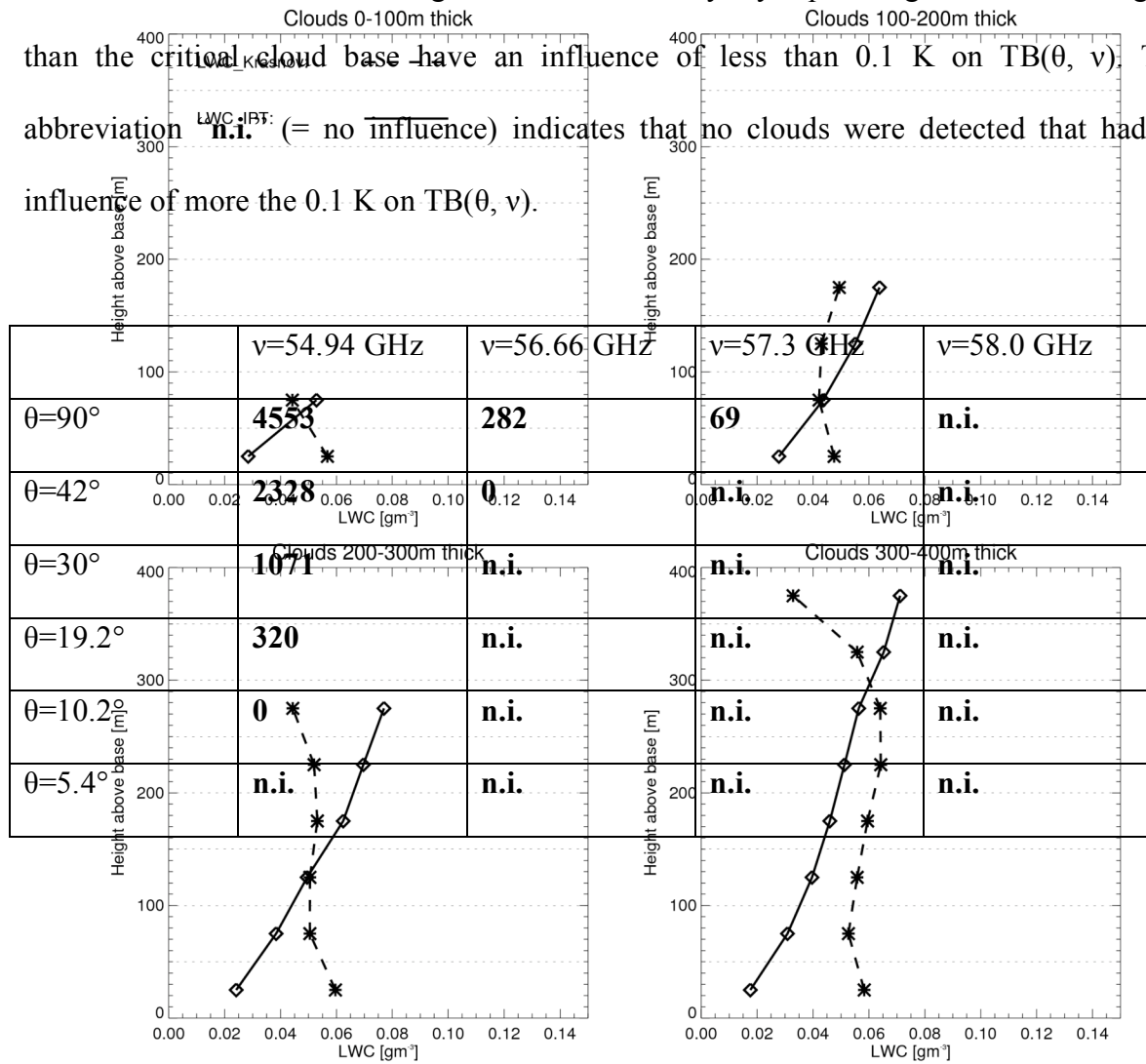|	ν=54.94 GHz	ν=56.66 GHz	ν=57.3 GHz	ν=58.0 GHz
θ=90°	**4553**	**282**	**69**	**n.i.**
θ=42°	**2328**	**0**	**n.i.**	**n.i.**
θ=30°	**1071**	**n.i.**	**n.i.**	**n.i.**
θ=19.2°	**320**	**n.i.**	**n.i.**	**n.i.**
θ=10.2°	**0**	**n.i.**	**n.i.**	**n.i.**
θ=5.4°	**n.i.**	**n.i.**	**n.i.**	**n.i.**

Fig. 8: Mean derived profiles of LWC from IPT and K06 during 13 days of the LAUNCH 2005 campaign. In order to be able to compare the results, clouds were binned into 4 categories of vertical extension (0-100m, 100-200m, 200-300m and 300-400m).

764

765

766

767

768

Tab. 2: a, b parameters used for the different cloud types (Z-LWC relationships, $Z = a\text{LWC}^b$).

Cloud type	Notation in Fig. 2	a	b	Reference
Cloud "without drizzle"	**F**	0.012	1.16	Fox and Illingworth (1997)
Cloud with "light drizzle"	**B**	57.54	5.17	Baedi et al. (2000)
Cloud with "heavy drizzle"	**K**	323.59	1.58	Krasnov and Russchenberg (2002)

769

770

771

772